Structural anisotropy and orientation-induced Casimir repulsion in fluids

Alexander P. McCauley,[1] F. S. S. Rosa,[2,3] Alejandro W. Rodriguez,[4,5] John D. Joannopoulos,[1] D. A. R. Dalvit,[3] and Steven G. Johnson[4]

[1]*Department of Physics, Massachusetts Institute of Technology, Cambridge, Massachusetts 02139, USA*
[2]*Laboratoire Charles Fabry, Institut d'Optique, CNRS, Université Paris-Sud, Campus Polytechnique, RD128, F-91127 Palaiseau Cedex, France*
[3]*Theoretical Division, Los Alamos National Laboratory, Los Alamos, New Mexico 87545, USA*
[4]*Department of Mathematics, Massachusetts Institute of Technology, Cambridge, Massachusetts 02139, USA*
[5]*School of Engineering and Applied Sciences, Harvard University, Cambridge, Massachusetts 02139, USA*

(Received 22 September 2010; published 10 May 2011)

In this work we theoretically consider the Casimir force between two periodic arrays of nanowires (both in vacuum, and on a substrate separated by a fluid) at separations comparable to the period. Specifically, we compute the dependence of the exact Casimir force between the arrays under both lateral translations and rotations. Although typically the force between such structures is well characterized by the proximity force approximation (PFA), we find that in the present case the microstructure modulates the force in a way qualitatively inconsistent with PFA. We find instead that effective-medium theory, in which the slabs are treated as homogeneous, anisotropic dielectrics, gives a surprisingly accurate picture of the force, down to separations of half the period. This includes a situation for identical, fluid-separated slabs in which the exact force changes sign with the orientation of the wire arrays, whereas PFA predicts attraction. We discuss the possibility of detecting these effects in experiments, concluding that this effect is strong enough to make detection possible in the near future.

DOI: 10.1103/PhysRevA.83.052503 PACS number(s): 31.30.jh, 12.20.Ds, 42.50.Lc

I. INTRODUCTION

Casimir forces are usually attractive interactions measurable at small separations, but recent theoretical works [1–8] have predicted a variety of situations in which these forces can be modified by using complex microstructures. In addition, by utilizing different choices of materials the Casimir force can be changed in both magnitude [9] and sign [10–12]. However, with some exceptions [7,8], the qualitative aspects of these effects can be explained through a combination or competition of forces calculated using some form of the proximity force approximation (PFA, a common heuristic description of the Casimir force as pairwise interactions between parallel surface patches) [13]. It is therefore of interest to consider situations in which geometry not only allows the Casimir force to be modulated (e.g., by reducing or changing the sign of the force), but also creates effects that cannot be accounted for by PFA.

In this paper, we introduce and examine a geometry that exhibits both of these qualities. We examine the configuration shown in Fig. 1, consisting of two identical microstructured slabs consisting of periodic arrays of dielectric nanowires. We compute the exact Casimir force for this geometry using a combination of existing scattering theory techniques [14–16], to be described below. We find that the microstructure of the slabs leads to a number of interesting qualitative effects: the force between the slabs can be dramatically modulated by rotating the two slabs at fixed surface-surface separation. In vacuum, the force between the slabs can be significantly reduced (more than halved as the rotation angle changes), and if the slabs are immersed in a fluid, the sign of the force can flip. It turns out that, even at moderate separations $d/a \sim 1$, PFA (an uncontrolled approximation) cannot capture either of these effects. Specifically, consider the behavior of the Casimir force between the slabs as they undergo lateral translations y (at $y = 0$ the slabs are mirror symmetric) and rotations θ. At $\theta = 0$, the slab microstructures are aligned, as shown in Fig. 1 (top), while for $\theta = \pi/2$ the slabs are crossed, as shown in Fig. 1 (bottom). As y and θ are varied, the slab surface-surface separation d is kept fixed. From a simple geometric argument, it is clear that for vacuum-separated wires PFA predicts the following bound on the Casimir force between two identical slabs:

$$F_{\text{aligned},\,y=a/2} \leqslant F_{\text{crossed}} \leqslant F_{\text{aligned},\,y=0} \tag{1}$$

(a positive force is attractive). Here F_{crossed} denotes the force when $\theta = \pi/2$. This bound is insensitive to the details of the exact PFA used, and simply relies on the fact that the wire surface-surface separations are minimized at $\theta = 0$, $y = 0$ and maximized when $\theta = 0, y = a/2$. Although a PFA prediction must be valid as $d/a \to 0$, for the systems examined in this work we find that the bound Eq. (1) is violated even at moderate distances $d/a \sim 1$. For vacuum-separated metallic or dielectric (e.g., gold or silica) nanowires and no substrate, this implies that changing the orientation of the wire arrays (i.e., their geometry) plays a stronger role in reducing the force than simply reducing the pairwise surface-surface separation between the slabs. In another case to be discussed, in which the wires are gold, the substrate silica, and the fluid ethanol, the bound equation (1) is also valid. However, we find from exact calculation that while PFA predicts $F_{y=a/2} < 0$ and $F_{\text{crossed}} > 0$, the opposite is in fact true, i.e., aligned slabs are always attracted to each other, while crossed slabs are *repelled*. Therefore, in our case at $d/a \sim 1$ the sign of the force can therefore be modulated by rotating the slabs (but not translating them), an interesting possibility for experiments that we discuss later.

To understand these effects qualitatively, we find that a much more suitable framework is the effective medium approximation (EMA), in which the microstructured slabs of Fig. 1 are describable as a homogeneous medium with a given anisotropic permittivity tensor $\overleftrightarrow{\varepsilon} = \text{diag}(\varepsilon_{||}, \varepsilon_{\perp}, \varepsilon_{\perp})$ (here

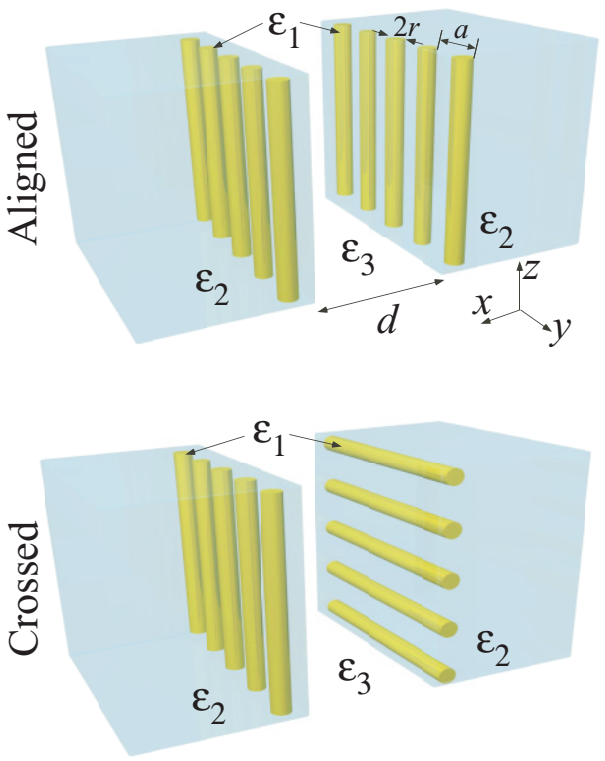

FIG. 1. (Color online) Configuration examined in the text. Each slab consists of a single periodic array of cylindrical wires embedded in a semi-infinite substrate; the goal is to create an effective anisotropic medium for each slab. Of interest here is the change in the force from when the wires are aligned (top) and when they are crossed (bottom). When the medium between the plates is a properly chosen fluid, we show that the force switches sign as a function of orientation for certain separations.

and below, $\overleftrightarrow{\varepsilon}$, $\varepsilon_{||}$, and $\varepsilon_{\perp}$ will be used to denote effective, homogenized permittivities). We are able to compute the effective ε tensor for this configuration from our scattering method [17], and we find that for the gold-silica-ethanol configuration, the deduced effective-medium parameters follow an ascending sequence $\varepsilon_{\perp} < \varepsilon_{\text{fluid}} < \varepsilon_{||}$. This ascending sequence is known to lead to repulsion [18] for uniform, isotropic materials, and we find below that the effect is also present for anisotropic materials and individual polarizations (although in this case, as discussed below, an ascending sequence is not sufficient for repulsion). One expects the EMA to be strictly valid as $d \to \infty$, however, in our case it turns out, somewhat surprisingly, to be qualitatively accurate down to $d/a \lesssim 1$. (A mathematical proof of why the EMA holds at such short separations, at least for crossed slabs, is given in Appendix B.) Further, we find that for realistic materials (gold wires, silica substrate, immersed in an ethanol fluid) and geometry parameters, this orientation-induced repulsion at fixed surface-surface separation between the two slabs holds down to separations $d/a \sim 0.5$.

Previous works [17,19] have discussed the possibility of using geometry to create artificial constitutive relations (e.g., effective permeability $|\overleftrightarrow{\mu}| > |\overleftrightarrow{\varepsilon}|$ [under a suitable matrix norm] to obtain Casimir repulsion or chirality $\kappa \neq 0$ to achieve force reduction). However, it has been rigorously proven [20] that no such media with $\overleftrightarrow{\mu} > \overleftrightarrow{\varepsilon}$ can be constructed from metallic/dielectric constituents so as to exhibit repulsion in vacuum, and computations involving the exact microstructures [21] have shown that chirality effects are only present at separations so large that they cannot conceivably be detected. Therefore, while in some circumstances EMA can be a useful qualitative guide (and rigorously accurate in certain limits), it must be used with caution—ideally, as a supplement to exact calculations. Orientation dependence (and the resulting Casimir torque) between slabs has previously been considered for two birefringent plates with weak anisotropy [22–24], and for corrugated metallic plates [2]. Although the torques in these systems are in principle measurable, the change in the force with orientation is small, and the forces are always attractive. reference [25] showed a large orientation dependence for theoretical uniaxial conductors, and suggested a possible realization via nanowire arrays, but without calculation in the latter case and without changing the sign of the force.

In the present work, we analyze this effect for periodically patterned, vacuum-separated suspended membranes (which form a potentially promising medium for Casimir force measurements [26]) and for gold wires on silica substrate, immersed in ethanol. In both cases, we find Eq. (1) is violated down to $d/a \sim 1$. In the former case, we find that the force is 70% lower for crossed slabs compared to aligned slabs (for any y) at large separations, while at separations comparable to the unit cell (e.g., 100 nm) there is a more modest, but still significant, 30% reduction. For the latter system, we find that aligned slabs are attractive for all y down to $d/a \sim 0.5$ while crossed slabs are repulsive in this range. These examples demonstrate a system in which effective-medium theory is correct and gives predictions that differ from PFA in a highly nontrivial way. Given that nanowire arrays below 15 nm can be fabricated with current technology [27] and that for these dimensions the predicted effects occur down to sub-100-nm-length scales, these effects should be experimentally accessible. After presenting these results, we argue how they may be experimentally detectable (assuming suitable fabrication techniques) and estimate force magnitudes in the hypothetical case where one of the slabs is replaced by either a sphere or cylinder with a wire pattern stamped on its surface.

II. METHOD

In this work, we perform Casimir force calculations with a semianalytic scattering method using a combination of results from Refs. [14–16], which efficiently computes the exact Casimir force between periodic arrays with one dimension of translation invariance. Our implementation differs somewhat from previous scattering methods (e.g., Refs. [28] and [29]) in that it is particularly well suited to unit cells with objects of compact cross section, such as the wires in Fig. 1 (rather than, e.g., extended rectangular gratings). While we are primarily interested in objects of circular cross section in the current work, the present method can be extended in a straightforward manner to treat unit cells with arbitrarily shaped compact objects using an existing boundary-element method [30,31].

In addition, we have checked the results with a brute-force finite-difference time-domain (FDTD) [32,33] method and found good agreement, and additionally, these computations show similar results for square wires. Also, the effects are not significantly different at zero temperature and 300 K, so we work exclusively in the former limit.

The two plates are separated from each other by a distance d in the x direction, and the slab is termed y directed if the wires are along the y axis (similarly for z). The slabs are aligned if both slabs are y or z directed, and crossed if they are not. The zero-temperature Casimir interaction energy for a q-directed slab displaced by $\mathbf{x}$ from a q'-directed slab ($q,q' = y,z$) is

$$E = \frac{\hbar c}{2\pi}\int_0^\infty d\xi \int \frac{d^2\mathbf{k}_{yz}}{4\pi^2} \ln\det\left(\mathbb{I} - \mathbb{R}_1^{(q')}\mathbb{U}^\dagger\mathbb{R}_2^{(q)}\mathbb{U}\right), \qquad (2)$$

where $\mathbb{R}_{1,2}$ are the scattering matrices of plane waves for the two slabs, $\mathbb{U}(\mathbf{x})$ is the plane-wave translation matrix for relative displacement $\mathbf{x}$ between the slabs, and the integral of transverse wave-vector components k_y,k_z is over the first Brillouin zone. See Ref. [16] for a detailed derivation and a partial review of precursors [34–36]. For the present work, we require an efficient method of computing the scattering matrices from periodic arrays, which we describe in more detail in Appendix A1.

For sufficiently large distances, the relevant frequencies and wave vectors are unable to probe the structure of the arrays and consequently, an effective-medium approximation should produce good results. In our case, such an effective medium should have a much larger conductivity in the direction of the wires as compared to the other orthogonal directions, even in the static limit (this being one of the motivations for the current configuration), so it is clear that an anisotropic EMA is called for. Fortunately, Casimir interactions between anisotropic homogeneous media have been studied by several authors [17,37–40], allowing us to build upon their results. We use the method of Ref. [17] (outlined in Appendix A 2) to obtain the scattering matrices assuming a known permittivity $\overleftrightarrow{\varepsilon}$. In the subsequent analysis, we also require the inverse procedure: given the scattering matrices (computed using the method of Appendix AA) of the exact structure, retrieve the best-fit EMA $\overleftrightarrow{\varepsilon}$. This procedure quickly becomes intractable if arbitrary $\overleftrightarrow{\varepsilon}$ and $\overleftrightarrow{\mu}$ are allowed. Instead, we assume $\mu_{ij} = \delta_{ij}$ and $\overleftrightarrow{\varepsilon}_{xx} = \overleftrightarrow{\varepsilon}_{yy}$ exhibit no dependence on $\mathbf{k}_\perp$ aside from its polarization. For $|\mathbf{k}_\perp| \to 0$ the scattering matrices for each polarization reduce to the standard Fresnel formula for reflection off isotropic interfaces. Their inversion then yields the effective dielectric tensor

$$\varepsilon_{||}(i\xi) = \varepsilon_{\text{fluid}}\left(\frac{1-R_{||}}{1+R_{||}}\right)^2, \quad \varepsilon_\perp(i\xi) = \varepsilon_{\text{fluid}}\left(\frac{1+R_\perp}{1-R_\perp}\right)^2. \qquad (3)$$

III. RESULTS

In the configuration of Fig. 1, the wires have radius $r = 0.3\,a$ and period a; we take the wire centers to be in the substrate and the wire surface to be tangent to the substrate surface to maximize the wire-wire interactions. The permittivities of wires, substrate, and fluid are, respectively, $\varepsilon_1(i\xi)$, $\varepsilon_2(i\xi)$, and $\varepsilon_3(i\xi)$ for imaginary frequency ξ. The materials used for the wires, substrate, and fluid are gold, ethanol, and silica, respectively. For gold, we use a plasma model with $\xi_p = 1.36\times10^{16}$ rad/s (the addition of a small loss term does not change the results significantly). For silica and ethanol we use standard oscillator models [41,42].

A. Vacuum-separated slabs

We first compute the Casimir forces when the intervening medium is vacuum ($\varepsilon_3 = 1$), comparing the force $F_{\text{aligned}}(y)$ for aligned slabs with the force F_{crossed} for crossed slabs. In the aligned case, the force can depend on y (leading to a lateral component of the force), and in this case F_{aligned} refers only to the *normal* component of this force. In the crossed case $\theta = \pi/2$ there is no y dependence. Although there is no sign change for vacuum-separated slabs, this configuration is of interest because it can be fabricated as a single suspended-membrane structure for each orientation [26], and may be easier to work with than a fluid system. Figure 2 shows results for wires composed of perfect metal, gold, and heavily doped silicon, the latter being more conventional for fabrication. We plot the ratio $F_{\text{crossed}}/F_{\text{aligned}}(y)$ (the shaded regions indicate the full range of this ratio as y is varied), which serves two purposes. First, it indicates the required relative accuracy in a force measurement needed to discern the orientation dependence of the force in an experiment. Second, it indicates the transition from the PFA to the EMA regimes via Eq. (1): if the force is determined as a sum of pairwise interactions, then the total force is maximized when the pairwise surface-surface distances are minimized. A simple geometric argument shows that the net distance is maximized for $\theta = 0$, $y = a/2$. On the

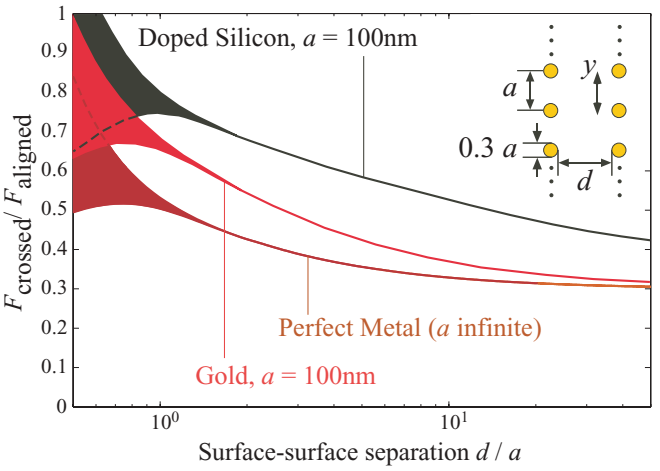

FIG. 2. (Color online) Ratio of the Casimir force between crossed wire arrays (F_{crossed}) over aligned wires [$F_{\text{aligned}}(y)$] between vacuum-separated nanowires of perfect metal, gold, and doped silicon (dopant density $10^{20}/\text{cm}^3$). $a \to \infty$ corresponds to using nondispersive $\varepsilon(i\xi \to 0)$ for all materials (because ξ is in units of c/a). Shaded regions indicate the range of values that F_{aligned} takes over all relative lateral displacements y of the wire centers, with their higher (lower) boundary indicating the force for $y = 0$ ($y = a/2$). PFA predicts, via Eq. (1), that the maximum of this ratio should exceed 1, which is only true for Si at $d/a \sim 0.6$, and for gold/perfect metal at lower separations. Inset: details of the configuration examined.

other hand, this distance is minimized for $\theta = 0$, $y = 0$. The bound equation (1) then follows. It turns out that the force is always attractive in this situation, so we have the further bound $F_{\text{aligned}}(y = a/2) > 0$. Therefore, PFA predicts that there is a range of y such that $F_{\text{crossed}}(y)/F_{\text{aligned}} > 1$. By contrast, EMA predicts the inequality $F_{\text{crossed}} < F_{\text{aligned}}$ (there is no y dependence in this approximation). This inequality stems from the following scattering-theory argument: for $d/a \gg 1$, the exponential suppression of $k_y, k_z \neq 0$ in $\mathbb{U}$ [16] implies that the force is dominated by the scattering of plane waves at normal incidence ($k_y = k_z = 0$). For normal incidence, the reflection matrix $\mathbb{R}^{(z)}$ is anisotropic but diagonal in polarization, and can be computed from an effective anisotropic dielectric tensor, $\overleftrightarrow{\varepsilon}(i\xi)$:

$$\overleftrightarrow{\varepsilon}(i\xi) = \text{diag}(\varepsilon_{xx}, \varepsilon_{yy}, \varepsilon_{zz}) \Rightarrow \mathbb{R} \approx \text{diag}(R_{||}, R_{\perp}), \qquad (4)$$

where $R_{||}$ and $R_{\perp}$ are the matrix elements for incident light polarized parallel and perpendicular, respectively, to the wires. For normal incidence, ε_{xx} does not contribute, and we define $\varepsilon_{||} = \varepsilon_{zz}$ and $\varepsilon_{\perp} = \varepsilon_{yy}$. Due to the high permittivity of the wires and the low permittivity of the substrate, we expect $|R_{\perp}| \ll |R_{||}|$ and $R_{\perp} R_{||} \geqslant 0$ [note that $R(i\xi)$ is real]. When the wires are aligned, the relevant product of scattering matrices in the energy integrand is $(R_{||}^2 + R_{\perp}^2) \approx R_{||}^2$, and when they are crossed the term is $2R_{||}R_{\perp}$, implying $F_{\text{crossed}} < F_{\text{aligned}}$. From Fig. 2, this bound is clearly violated in doped Si for $d/a < 0.6$, and for other materials at smaller d. Note that this includes a region $d/a < 2$ for which there is still a strong y dependence of this ratio, indicating that while EMA is not strictly valid, it still has more predictive power than PFA.

As $d/a \to \infty$, the force ratios should approach a constant determined by $\overleftrightarrow{\varepsilon}(\xi \to 0)$: this ratio is ≈ 0.29 for all three materials. However, this limit is approached very slowly [$O(d^{-1/2})$ for perfect metal/gold wires]. The EMA d dependence is due both to constituent material dispersion and an effective geometric dispersion in $\overleftrightarrow{\varepsilon}(i\xi)$ induced by the geometry of the wires. As $\xi \to 0$, $\varepsilon_{||} \to \varepsilon_1(i\xi)$ and $\varepsilon_{\perp} \to \varepsilon_2(i\xi)$. The former limit follows from the $1/\xi^2$ divergence of ε_1 as $\xi \to 0$ (if we add a dissipative term to ε_1, the divergence is only $1/\xi$ but this crossover occurs at frequencies too low to affect the present results). The latter limit follows from the fact that the static polarizability of the wires in the transverse direction is finite, implying that their contribution to the scattering amplitude vanishes as $\xi \to 0$. Therefore, as $\xi \to 0$, $\varepsilon_{\perp}$ depends only on the substrate, which has semi-infinite extent; we have checked this relation numerically and found good agreement. $\lim_{d\to\infty} F_{\text{crossed}}/F_{\text{aligned}}$ can then be obtained by computing the force between two anisotropic plates, with $\varepsilon_{||} = \infty$ and $\varepsilon_{\perp} = \varepsilon_2(0)$.

For all $d/a \gg 1.5$, the orientation dependence of the force is quite strong ($\gg$30%). In this range, the absolute pressure is approximately 2% of the corresponding pressure between two homogeneous perfect metal plates. As differences of this magnitude between vacuum-separated plates have been measured on the 100-nm-length scale, we are hopeful that this departure from PFA can be detected experimentally.

B. Fluid-separated slabs and tunable repulsion

In the previous example the force is always attractive, because $\varepsilon_1(i\xi), \varepsilon_2(i\xi) \geqslant \varepsilon_3(i\xi)$ for all ξ [20]. However, if the medium between the slabs is a fluid such that $\varepsilon_1(i\xi) > \varepsilon_3(i\xi) > \varepsilon_2(i\xi)$, the above EMA analysis predicts that the force in the crossed configuration should be repulsive as $d/a \to \infty$ since by the Fresnel formula at $\xi = 0$, $R_{\perp} R_{||} < 0$, leading to the well-known Casimir repulsion for an ascending sequence of ε for each polarization [11]. By contrast, in the aligned configuration the force is attractive when $y = 0$ due to mirror symmetry [43], and the intuition that this attraction holds for nonzero y is confirmed by calculation. However, strong corrections to this argument occur at finite separations: waves with nonzero k_y and k_z contribute, and are not in general polarized along the y or z axes. These waves will couple to both $\varepsilon_{||}$ and $\varepsilon_{\perp}$ on each reflection. The sign of the resultant reflection coefficient will usually be the same for both z- and y-directed slabs, leading to attractive contributions. Further, the microstructure can also lead to significant corrections, possibly eliminating the effect for separations comparable to the unit cell a [21]. As such separations are necessarily required for experiments, we require exact results to verify that this effect persists in experimentally accessible regions.

The exact results are shown in Fig. 3; as in Fig. 2, shaded regions show the y dependence. The results show a clear attractive-repulsive transition as the slab orientation is varied between the aligned and crossed configurations. This effect persists for both the ideal case of perfect metals ($a \to \infty$) and dispersive materials at $a = 100$ nm; both show qualitatively similar behavior. For crossed slabs, the repulsion is fairly flat over an $\sim$40 nm range. At first sight, it is tempting to ascribe the repulsive force observed for crossed wires to PFA-line interactions between opposing areas where metallic wires face a dielectric substrate and thus feel a repulsive force. However, if this were the case, then by the same argument [and Eq. (1)],

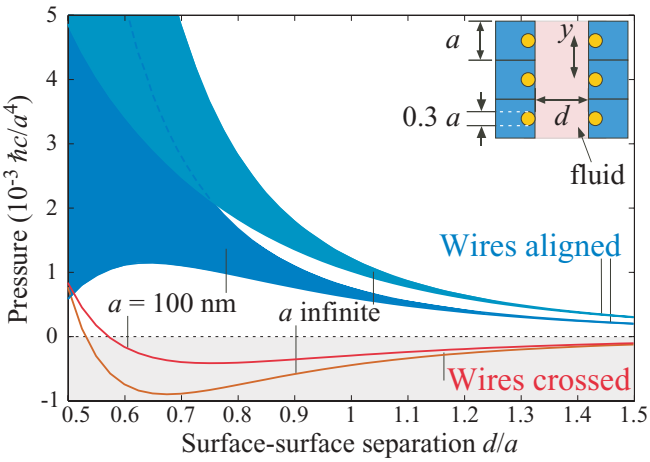

FIG. 3. (Color online) Casimir pressure for the same parameters as the inset of Fig. 2, with a silica substrate and ethanol between the two slabs. Positive values indicate an attractive force, negative values (shaded) repulsive. Both $a \to \infty$ and $a = 100$ nm are shown. As in Fig. 2, shaded regions denote the range of y displacements. When the wires are aligned (blue), the force is always attractive, but when the wires are crossed (red), the force turns repulsive at a critical separation $d > d_c$, which depends on a.

$F_{\text{aligned}}(y = a/2)$ should exhibit an even stronger repulsion. This is clearly not the case in Fig. 3 for $d/a > 0.5$; rather, the results for repulsion are consistent with the EMA argument given above. To estimate the magnitude of this repulsion, for $a = 100$ nm the repulsive pressure is approximately 1% of the pressure between parallel perfectly conducting plates separated by a comparable distance d in vacuum, e.g, ~ 0.13 pN/μm^2. Repulsive forces in fluids on this order of magnitude have been measured [11], therefore these forces are potentially within reach of current or near-future measurement techniques (the force in more realistic sphere-plate and cylinder-plate geometries will be considered in Sec. III D below). Interestingly, when the wires are crossed and d varies there is an attractive-repulsive transition at a critical separation $d = d_c$. This leads to an unstable equilibrium with respect to d. (The crossed configuration is always unstable with respect to orientation.) This transition, as mentioned above, is attributed to the eventual dominance of attractive forces as separation goes to zero. However, we will see below that such a transition is predicted by EMA as well, and is therefore not due entirely to proximity effects.

Before continuing, it is interesting to see what the PFA prediction for the force in this system is. We simplify matters by computing the PFA assuming instead wires of a square $r \times r$ cross section, with centers a distance $r/2$ beneath the substrate surface (by minimizing the amount of curved surface, we expect this to maximize the range of separations for which PFA is accurate). Using FDTD computations [32,33], we have found that this system exhibits behavior qualitatively similar to that of Fig. 3. The results for $a = 100$ nm are shown in Fig. 4 (taking $a \to \infty$ yields a qualitatively similar curve). Inspection reveals that the PFA prediction exhibits the *opposite* behavior for the sign of the force as the full numerical calculations: the PFA force is exclusively *attractive* for crossed wires, but for aligned wires shifted by $y = a/2$ the force becomes *repulsive*.

Although PFA fails qualitatively and quantitatively to predict the results of Figs. 2 and 3, we have not yet examined the quantitative accuracy of EMA. In the next section, we will examine a description of the force in terms of the EMA, rigorously valid in the regime ($d/a \to \infty$). We will see that EMA gives qualitatively correct predictions for the magnitude and sign of the forces down to separations comparable to the unit-cell size.

C. Comparison with EMA

In this section, we examine the extent to which the EMA analysis given above in Sec. III A predicts the correct results, using the method of Appendix A 2. We use a simplified EMA, assuming that $\overleftrightarrow{\mu}(i\xi) = 1$ and $\overleftrightarrow{\varepsilon}(i\xi)$ is isotropic in the plane perpendicular to the wires. In this case, $\varepsilon_{||}$ and $\varepsilon_{\perp}$ are the only EMA parameters involved; these are retrieved by applying Eq. (3) to the scattering matrices computed from the exact structure. The EMA-predicted force is then computed from the method of Appendix A2. A plot of the retrieved parameters for $a = 100$ nm is shown in Fig. 5. Shown for reference in Fig. 5 are $\varepsilon(i\xi)$ of the constituent materials ethanol, silica, and gold. As expected, $\varepsilon_{\perp}$ approaches $\varepsilon_{\text{silica}}$ for low ξ, while for higher ξ the wires increase the effective permittivity. In $\varepsilon_{||}$, we see a significant geometric dispersion: in fact, at low ξ, $\varepsilon_{||}(i\xi) \sim 1 + (\xi'_p/\xi)^2$, where $\xi'_p \sim 0.36\,\xi_p$ is a new, effective plasma frequency for the gold wires. This is similar to an argument presented in Ref. [44], where the effective dielectrics of square arrays of wires along the wire axis can be described by a plasma model with a reduced plasma frequency (as we have only included a single row of wires, the result of Ref. [44] cannot be directly applied, but its basic idea remains). A similar

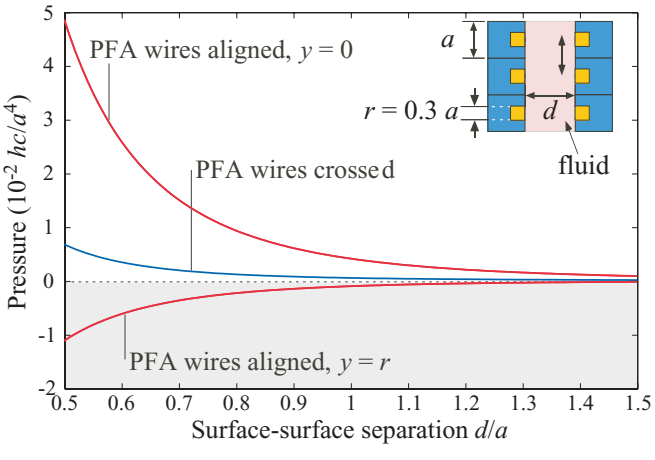

FIG. 4. (Color online) Forces computed for the configuration of Fig. 3 using the proximity force approximation (PFA), for $a = 100$ nm. For convenience in applying the PFA, square wires of width r are used instead of circular wires (the exact results are not qualitatively changed). We see that the behavior of Fig. 3 is not qualitatively captured: the force is always attractive for crossed wires, and the bound Eq. (1) is strictly satisfied. Similar results are obtained for $a \to \infty$.

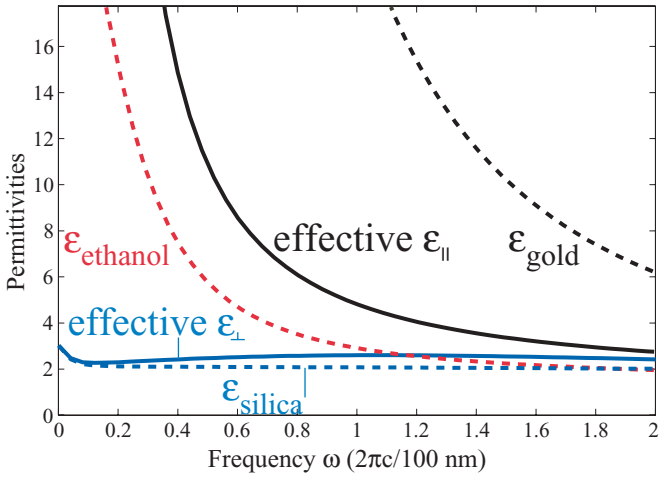

FIG. 5. (Color online) Effective-medium parameters for the system of Fig. 3 derived from scattering data for a length scale $a = 100$ nm. $\varepsilon_{||}$ is the effective dielectric parallel to the wires (black), and $\varepsilon_{\perp}$ is the effective dielectric perpendicular to the wires (blue). The dielectrics of the constituent materials gold, silica, and ethanol are shown for reference. These dispersions will be used to compute the Casimir force in the effective-medium approximation below.

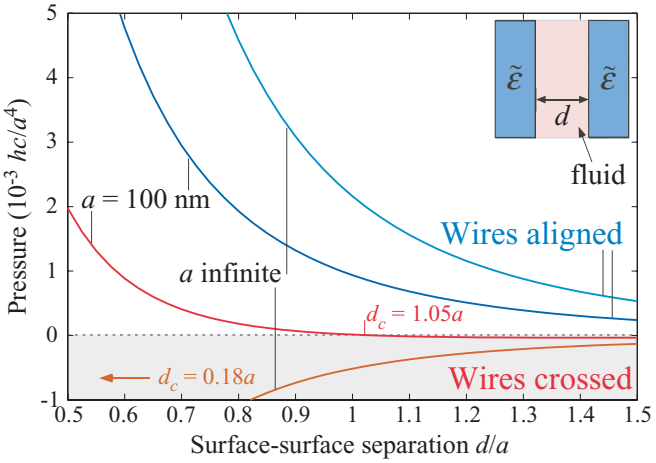

FIG. 6. (Color online) Results for the force computed in the effective-medium approximation (EMA) using an effective homogeneous, anisotropic permittivity tensor $\overleftrightarrow{\varepsilon}$, via the method described in Appendix A2. As in Fig. 3, results for both a infinite (i.e., nondispersive materials) and $a = 100$ nm are shown, for both crossed and aligned configurations. Although quantitatively inaccurate over the range plotted, the EMA does qualitatively capture the behavior of the force as opposed to PFA. Also shown are d_c, the location of the attractive-repulsive transitions for the crossed wires ($d_c = 0.18a$ for $a \to \infty$ and is not shown).

effect holds when the wires are perfect conductors, where $\xi_p' = 7.9$. This accounts for the d dependence in the EMA regime of Fig. 2: the geometry introduces an effective length scale into the system, given by ξ_p.

We use the retrieved $\varepsilon_{||}$ and $\varepsilon_\perp$ to compute $\mathbb{R}$ and hence the Casimir force for the fluid-separated geometry. Computation of the force with the EMA parameters for the vacuum-separated slabs in the limit $d \to \infty$ is in agreement with the results of Fig. 2. The results for the fluid-separated case are shown in Fig. 6. We find that, as opposed to PFA, EMA gives qualitatively accurate (i.e., the same order of magnitude) predictions for both the magnitude and sign of the force. In particular, EMA predicts attractive-repulsive transitions at some $d = d_c$, where for $d < d_c$ the force for crossed slabs is attractive. The fact that $\varepsilon_{||}(\xi)$ is a rapidly decreasing function of ξ, while $\varepsilon_\perp$ increases, indicates that within the EMA the force should receive attractive contributions from higher ξ (which dominate at small separations). Further, the decrease of both $\varepsilon_{||}$ and ε_2 with decreasing a also contributes to a reduction in repulsion. This explains why the repulsion for $a = 100$ nm is lower than for $a \to \infty$. With our simplified EMA the predicted values of d_c are very inaccurate: $d_c \approx 0.18\,a$ for $a = \infty$ and $d_c \approx 1.05\,a$ when $a = 100$ nm. However, the y-independent regimes of Figs. 2 and 3 suggest that some EMA must be valid in those regimes, and in this case a more accurate EMA would involve both $\varepsilon_{xx} \neq \varepsilon_\perp$ as well as an anisotropic effective $\overleftrightarrow{\mu}$. A more general model of dispersion would allow for a translation-invariant but $\mathbf{k}$-dependent permittivity. Fitting an effective $\overleftrightarrow{\varepsilon}(\mathbf{k})$ is somewhat complicated in this framework; rather, to explore the validity of this "specular" approximation we compute the force with all nonspecular (i.e., terms not conserving $\mathbf{k}_\perp + \mathbf{G}_\perp$, where $\mathbf{G}_\perp$ is a reciprocal lattice vector) terms in the scattering matrix $\mathbb{R}$ removed. We find the surprising result that, while this specular approximation does not give significantly different predictions for the force for aligned wires, it gives much more accurate predictions for d_c and the magnitudes of the force for crossed wires. This indicates that nonspecular scattering events are suppressed when the wires are crossed, even at relatively small separations $d/a \sim 0.5$. We give a rigorous proof of this result in Appendix B, using a recently developed diagrammatic expansion for the Casimir energy [45].

D. Forces for other geometries

Parallel-plate configurations involving suspended membrane structures show potential for new sets of experimental Casimir force measurements for vacuum-separated geometries [26]; such measurements detect the Casimir force (or force gradient) through a shift in either the optical spectrum or the resonance frequency of the upper membrane. However, to measure the sign change in the force predicted here a measurement between fluid-separated objects must be performed, where fluid damping is prohibitive. Instead, a force measurement involving an object (e.g., a sphere) mounted on an atomic force microscope (AFM) tip [11] is more realistic. In this case, alignment issues favor the use of one spherical and one planar object [46,47], rather than the two planes considered here. For our purpose, a pattern of wires similar to Fig. 1 would need to be stamped on the surface of the object. In this section, we give force predictions for both sphere-plate and cylinder-plate geometries. The latter case has more difficult alignment issues, but is still simpler than plate-plate alignment, and in this case the Casimir force is much larger than for sphere-plate setups [48]. For both cases, the radius of curvature R is many orders of magnitude larger than the surface-surface separation d (e.g., $R = 200$ μm and $d \sim 100$ nm). Because $d,a \ll R$, it is appropriate to use a hybrid PFA/exact method in which each unit of surface on the sphere or cylinder feels the *exact* pressure (as computed in Sec. III B) between a plate-plate configuration of the same surface-surface separation. The result is asymptotically exact in the limit $R \to \infty$ for fixed d and a.

Results are shown in Fig. 7 for $R = 200$ μm and are plotted in units of piconewtons. The sphere-plate force has a peak repulsion of $\sim$10 pN, which although below the detection limit of current measurement techniques in fluids, may be observable in the near future. We also note that, although the presence of Casimir repulsion may be experimentally challenging, Eq. (1) can be verified with much less sensitivity (e.g., $\sim$50 pN at $d = 50$ nm). For the cylinder plate, we take a length $L = 16$ μm in order for the force to be comparable in magnitude to the sphere-plate force. However, it is clear that if we instead take $L \sim R$, we can obtain both repulsive and attractive forces on the order of 10^3 pN, well within current experimental detection ranges. Therefore, this system seems most attractive for detection of an attractive-repulsive transition with orientation in a fluid if techniques similar to those of Ref. [49] to align the long axis of the cylinder relative to the plane can be extended to fluid-separated objects.

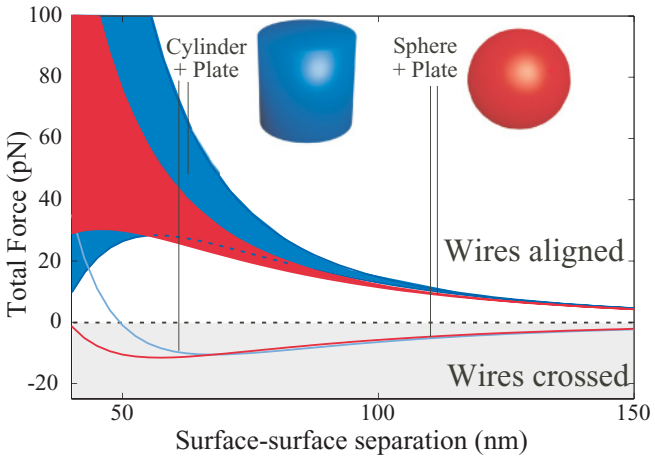

FIG. 7. (Color online) Forces for sphere-plate (red) and cylinder-plate configurations, for $a = 100$ nm. In both cases, the wire pattern of Fig. 1 is stamped onto the surface of both objects, which have radii of curvature $R = 200$ μm. The cylinder length is chosen to be $L = 16$ μm so that the two force curves have comparable magnitude; however, the cylinder-plate force is proportional to L and so will be much larger in magnitude for a more realistic $L \sim R$.

IV. CONCLUSIONS

We have presented an example system, consisting of microstructured slabs, in which PFA fails at relatively small separations. Instead, EMA qualitatively describes the behavior of the Casimir force, including the case in which the force can be switched from attractive to repulsive as the slabs are rotated. We have discussed the prospects for detecting these forces in experiments. One issue arising in an experiment, not discussed here, is the increased complexity of the electrostatic calibrations. Conceivably, these complications can be eliminated in the fluid-separated case by the addition of electrolytes to the fluid. This should also reduce or eliminate the effect of accumulated surface charges on the gold-silica interface, due to contact potentials [50,51]. For the case of vacuum-separated doped silicon, a more involved calibration procedure is required.

Although not examined here, we also note that orientational attractive-repulsive transitions may also occur using naturally anisotropic materials. We have confirmed this for the case of lithium niobate slabs immersed in ethanol at zero temperature; although here $d_c > 7$ μm (implying that finite-temperature effects must be taken into account), transitions at smaller separations may be possible with appropriate materials.

ACKNOWLEDGMENTS

We thank D. Woolf, J. Munday, F. Intravaia, and M. Maghrebi for useful discussions, and R. Zhao and K. Berggren for helpful references. This work was supported by the Army Research Office through the ISN under Contract No. W911NF-07-D-0004, and by DARPA under Contract No. N66001-09-1-2070-DOD and under DOE/NNSA Contract No. DE-AC52-06NA25396.

APPENDIX A: DETAILS OF COMPUTATIONAL METHODS

1. Scattering from periodic arrays

There are numerous computational and semianalytical methods from classical electromagnetic scattering that can be adapted to Casimir calculations [52]. For example, there are computational techniques based on generic grids/meshes, e.g., finite-difference methods [32,33,53,54]. There are also Casimir methods [28,29] based on classical cross-section methods (rigorous coupled-wave analysis [55], also called eigenmode expansion [56]), which divide the geometry into slices with constant cross sections and match modal expansions between slices. Alternatively, there are spectral integral-equation methods tracing their roots to classic Mie scattering and related problems [57]: one divides the geometry into high-symmetry objects such as spheres and cylinders, computing the scattering matrix for each object in a specialized basis (e.g., spherical waves), and then combining the matrices from different objects to match the boundary conditions. These methods have been adapted to Casimir problems for geometries consisting of a finite number of isolated objects [16,34–36] and corrugated surfaces [58]. Here, we adapt similar methods to periodic arrays of isolated objects (cylinders) by exploiting classical lattice-sum scattering methods [15]. For completeness, and because our formulation is directly in imaginary frequency and our normalization conventions differ from other applications [14,15], we outline the derivation in this section.

The scattering matrix $\mathbb{T}_0$ from a single circular cylinder can be computed analytically in the basis of cylindrical multipoles, using the basis functions [16]

$$|\mathbf{E}\rangle_{k_z,n}^{p,\mathrm{reg/out}}(i\xi,\mathbf{x}) = \mathbb{L}^p\left[\phi_{k_z,n}^{\mathrm{reg/out}}(i\xi,\mathbf{x}-\mathbf{x}_j)\hat{\mathbf{z}}\right], \quad \text{(A1)}$$

where the linear differential operators $\mathbb{L}^p$ ($p = M,N$ are the transverse electric and transverse magnetic polarizations, respectively) are

$$\mathbb{L}^M = \frac{1}{\sqrt{k_z^2+\xi^2}}\nabla\times,$$
$$\mathbb{L}^N = \frac{1}{\xi\sqrt{k_z^2+\xi^2}}\nabla\times\nabla\times,$$

and the cylindrical wave functions are

$$\phi_{k_z,n}^{\mathrm{reg}}(i\xi,\mathbf{x}) = I_n\left(\sqrt{k_z^2+\xi^2}\sqrt{x^2+y^2}\right)e^{ik_z z+in\theta},$$
$$\phi_{k_z,n}^{\mathrm{out}}(i\xi,\mathbf{x}) = K_n\left(\sqrt{k_z^2+\xi^2}\sqrt{x^2+y^2}\right)e^{ik_z z+in\theta}.$$

I_n and K_n are the modified cylindrical Bessel functions, and $\mathbf{x}_j$ gives the coordinate origin. The calculation of $\mathbb{T}_0$ is straightforward and we omit it here. We note that although the present method is simplified by the semianalytic calculation of the scattering from circular cylinders, methods exist that can compute the scattering matrices of noncircular cylinders of arbitrary cross section [31]; such a hybrid method allows for efficient scattering computations from general two-dimensional arrays of compact objects.

We now derive the scattering matrix $\mathbb{T}$ for a periodic array of cylindrical scatters in a uniform medium (the fluid interface will be added later). $\mathbb{T}$ is defined to be the scattering matrix

from each cylinder j in the basis given by Eq. (A1) with origin $\mathbf{x}_j = ja\hat{\mathbf{y}}$, in the presence of the entire array of cylinders. This array has period a in the y direction and is translation-invariant in z, and only a single layer in the x direction. In other words, for an incident field $|\mathbf{E}\rangle^{\text{in}}$, the scattered field emitted by currents on cylinder j is

$$|\mathbf{E}^{(j)}\rangle^{\text{scatt}} = e^{ik_y ja}\mathbb{T}|\mathbf{E}\rangle^{\text{in}}. \tag{A2}$$

Here we have assumed that the incident field $|\mathbf{E}\rangle^{\text{in}}$ is a plane wave with transverse wave-vector components k_y and k_z, and have normalized it with respect to the origin. Then using the translation matrices [16] for the basis functions of Eq. (A1), the scattered field from object j, converted to the basis at the origin ($j = 0$), is given by

$$\overset{p,\text{reg}}{k_z,n}\langle\mathbf{E}^{(j=0)}|\mathbf{E}^{(j)}\rangle = \sum_{n'',n'}\mathbf{S}^{(j)}_{n-n'}e^{ik_y ja}(-1)^{n'}\mathbb{T}^{p,p'}_{n',n''}{}^{p'}_{n''}\langle\mathbf{E}|\mathbf{E}\rangle^{\text{in}}, \tag{A3}$$

where the elements of the lattice sum $\mathbf{S}$ are given by

$$S^{(j)}_m = K_m\left(|\mathbf{x}|\sqrt{k_z^2+\varepsilon_2\xi^2}\right)e^{-im\theta_j} \tag{A4}$$

and $\theta_j = \text{sgn}(j)\frac{\pi}{2}$; and this transformation is diagonal in polarization p. Using linearity of the scattering process to sum over all incident cylindrical waves, the total incoming field at the origin x_0 for a plane wave $|\mathbf{E}\rangle^{\text{in}}$ is obtained by summing the incident fields and the scattered fields from all cells $j \neq 0$:

$$\begin{aligned}|\mathbf{E}\rangle^{\text{in,total}} &= \left[1+\left(\sum_{j\neq 0}e^{ik_y ja}\mathbb{S}^{(j)}\right)\mathbb{A}\mathbb{T}\right]|\mathbf{E}\rangle^{\text{in}}\\ &= (1+\mathbb{S}\mathbb{A}\mathbb{T})|\mathbf{E}\rangle^{\text{in}}.\end{aligned}$$

The matrix $\mathbb{S}$ is formally defined as the infinite sum of all $\mathbb{S}^{(j)}$ (in imaginary frequency this sum is well defined due to the exponential decay of K_n), and $\mathbb{A}_{n,n'} = (-1)^n\delta_{n,n'}$. The field scattered from the cylinder at $\mathbf{x} = \mathbf{x}_0$, in the presence of the array of cylinders, is then

$$|\mathbf{E}^{(j=0)}\rangle^{\text{scatt}} = \mathbb{T}_0(1+\mathbb{S}\mathbb{A}\mathbb{T})|\mathbf{E}\rangle^{\text{in}} = \mathbb{T}|\mathbf{E}\rangle^{\text{in}},$$

where the last equality follows by the definition of $\mathbb{T}$. Because this equation holds for arbitrary incident field vectors $|\mathbf{E}\rangle^{\text{in}}$, the equation holds for the operators as well, allowing us to solve for $\mathbb{T}$:

$$\mathbb{T} = [1-\mathbb{T}_0\mathbb{S}\mathbb{A}]^{-1}\mathbb{T}_0. \tag{A5}$$

Although both $\mathbb{S}$ and $\mathbb{A}$ are diagonal in polarization p, in general, $\mathbb{T}_0$ is not and different polarizations will couple to the periodicity via Eq. (A5). The scattering matrix from the entire array is a sum of $\mathbb{T}$ over all unit cells. This sum is more naturally expressed in a plane-wave basis, using the wave conversion matrices $\mathbb{D}$ for cylindrical waves [16] (here we have absorbed the normalization factors C_p, defined in Appendix B of Ref. [16], into the definition of $\mathbb{D}$), from which we find the plane-wave scattering matrix:

$$\mathbb{R}_{\mathbf{k}} = \mathbb{D}^{\dagger}_{\mathbf{k}}\mathbb{T}\mathbb{D}_{\mathbf{K}}. \tag{A6}$$

Here $\mathbf{k}$ is the reduced Bloch vector, and the matrix $\mathbb{R}_{\mathbf{k}}$ couples all vectors $\mathbf{k}+m\pi\hat{\mathbf{y}}$ for all integer m.

The incorporation of multiple interfaces in the x direction is achieved via a standard transfer-matrix approach, e.g., Ref. [15]. For the case of a uniform medium ε_3 outside of the plates, the Fresnel formula is combined in a straightforward manner with the matrix $\mathbb{T}$ above to finally give the full scattering matrix $\mathbb{R}$ for the objects of Fig. 1.

For numerical computations, ten cylindrical multipole moments in the single-cylinder scattering matrix, $10/\xi$ terms in the lattice sum of Eq. (A5), and a simple exponential extrapolation from only 7×7 Brillouin zones for Eq. (A6) were sufficient for $<1\%$ error.

2. Effective-medium approximation

In this section we outline the method used to predict the scattering matrices $\mathbb{R}$ from a specified $\overleftrightarrow{\varepsilon}$. The method is given in full detail in Ref. [17].

In an anisotropic EMA, we assume that the ith object is described by a homogeneous (position-independent) permittivity tensor

$$\overleftrightarrow{\varepsilon} = \begin{bmatrix}\varepsilon_{xx} & \varepsilon_{xy} & \varepsilon_{xz}\\ \varepsilon_{xy} & \varepsilon_{yy} & \varepsilon_{yz}\\ \varepsilon_{xz} & \varepsilon_{yz} & \varepsilon_{zz}\end{bmatrix}, \tag{A7}$$

where the frequency dependence is left implicit and we used the fact that the permittivity tensor is symmetric on its spatial indices [59]. The relatively symmetric character of our setup leads to a very useful simplification in Eq. (A7) that becomes apparent in a coordinate system with its z axis perpendicular to the slab interfaces: it is clear that regardless of the in-plane orientation of the wires there is no mixing with the z component, and so

$$\varepsilon_{xz} = \varepsilon_{yz} = 0. \tag{A8}$$

In addition, for our simplified EMA we make the further approximation that $\varepsilon_{xx} = \varepsilon_{yy} \equiv \varepsilon_{\perp}$. This symmetry implies that the ε tensor is diagonal in the x,y,z coordinate system of Fig. 1 (top) and is of the form

$$\overleftrightarrow{\varepsilon} = \begin{bmatrix}\varepsilon_{\perp} & 0 & 0\\ 0 & \varepsilon_{\perp} & 0\\ 0 & 0 & \varepsilon_{||}\end{bmatrix}. \tag{A9}$$

Consider a plane wave of transverse wave vector $\mathbf{k}_{\perp} = (k_y,k_z)$ impinging on the slab, and let ϕ be the angle $\mathbf{k}_{\perp}$ makes with the z axis. For our purpose, the scattering problem is best solved in the coordinate system (x',y',z') of the plane wave, where $x' = x$ and z' is parallel to $\mathbf{k}_{\perp}$. In this basis, the $\overleftrightarrow{\varepsilon}$ tensor becomes

$$\overleftrightarrow{\varepsilon} = \begin{bmatrix}\varepsilon_{\perp} & 0 & 0\\ 0 & \varepsilon_{\perp}c^2+\varepsilon_{||}s^2 & (\varepsilon_{||}-\varepsilon_{\perp})sc\\ 0 & (\varepsilon_{||}-\varepsilon_{\perp})sc & \varepsilon_{||}c^2+\varepsilon_{\perp}s^2\end{bmatrix},$$

where $c = \cos\phi$ and $s = \sin\phi$.

We can now proceed to determine the scattering matrices of plane waves for the isotropic-anisotropic flat interface. After a considerably long algebraic calculation (for details see Ref. [17], but note the change in coordinate systems between our Fig. 1 and their Fig. 3, and that for us $c = \cos\phi$ and the

speed of light is set to 1), it is possible to show that the four reflected/incident amplitude ratios are given by

$$r^{\mathrm{TE,TE}}(i\xi,\mathbf{k}_\perp) = \left.\frac{\det \mathbb{M}_1}{\det \mathbb{M}}\right|_{\substack{\omega\to i\xi \\ k_{z'}\to k_\perp}},$$

$$r^{\mathrm{TM,TE}}(i\xi,\mathbf{k}_\perp) = \left.\frac{\det \mathbb{M}_2}{\det \mathbb{M}}\right|_{\substack{\omega\to i\xi \\ k_{z'}\to k_\perp}},$$

$$r^{\mathrm{TE,TM}}(i\xi,\mathbf{k}_\perp) = \left.\frac{\det \mathbb{M}_3}{\det \mathbb{M}}\right|_{\substack{\omega\to i\xi \\ k_{z'}\to k_\perp}},$$

$$r^{\mathrm{TM,TM}}(i\xi,\mathbf{k}_\perp) = \left.\frac{\det \mathbb{M}_4}{\det \mathbb{M}}\right|_{\substack{\omega\to i\xi \\ k_{z'}\to k_\perp}},$$

where

$$\mathbb{M} = \begin{bmatrix} -1 & 0 & \alpha^{(1)} & \alpha^{(2)} \\ q_{\mathrm{in}}/\omega & 0 & -\beta^{(1)} & -\beta^{(2)} \\ 0 & q_{\mathrm{in}}/\omega & 1 & 1 \\ 0 & -1 & \gamma^{(1)} & \gamma^{(2)} \end{bmatrix},$$

$$\mathbb{M}_1 = \begin{bmatrix} 1 & 0 & \alpha^{(1)} & \alpha^{(2)} \\ q_{\mathrm{in}}/\omega & 0 & -\beta^{(1)} & -\beta^{(2)} \\ 0 & q_{\mathrm{in}}/\omega & 1 & 1 \\ 0 & -1 & \gamma^{(1)} & \gamma^{(2)} \end{bmatrix},$$

$$\mathbb{M}_2 = \begin{bmatrix} -1 & 1 & \alpha^{(1)} & \alpha^{(2)} \\ q_{\mathrm{in}}/\omega & q_{\mathrm{in}}/\omega & -\beta^{(1)} & -\beta^{(2)} \\ 0 & 0 & 1 & 1 \\ 0 & 0 & \gamma^{(1)} & \gamma^{(2)} \end{bmatrix},$$

$$\mathbb{M}_3 = \begin{bmatrix} 0 & 0 & \alpha^{(1)} & \alpha^{(2)} \\ 0 & 0 & -\beta^{(1)} & -\beta^{(2)} \\ q_{\mathrm{in}}/\omega & q_{\mathrm{in}}/\omega & 1 & 1 \\ 1 & -1 & \gamma^{(1)} & \gamma^{(2)} \end{bmatrix},$$

$$\mathbb{M}_4 = \begin{bmatrix} -1 & 0 & \alpha^{(1)} & \alpha^{(2)} \\ q_{\mathrm{in}}/\omega & 0 & -\beta^{(1)} & -\beta^{(2)} \\ 0 & q_{\mathrm{in}}/\omega & 1 & 1 \\ 0 & 1 & \gamma^{(1)} & \gamma^{(2)} \end{bmatrix}.$$

Here $q_{\mathrm{in}} \equiv \sqrt{\omega^2 - \mathbf{k}_\perp^2}$; the coefficients in the matrices above are defined by

$$\alpha^{(p)} = \frac{(q^{(p)})^2 - \omega^2 A}{\omega^2 C_1},$$
$$\beta^{(p)} = -\omega\frac{L_{31}}{q^{(p)}} - \omega\frac{L_{32}}{q^{(p)}}\alpha^{(p)}, \qquad \text{(A10)}$$
$$\gamma^{(p)} = -\omega\frac{L_{41}}{q^{(p)}} - \omega\frac{L_{42}}{q^{(p)}}\alpha^{(p)},$$

where $p = 1,2$ and also

$$q^{(p)} = q^{(\pm)} = \omega\frac{1}{\sqrt{2}}\sqrt{A + B \pm \sqrt{(A-B)^2 + 4C}}, \qquad \text{(A11)}$$

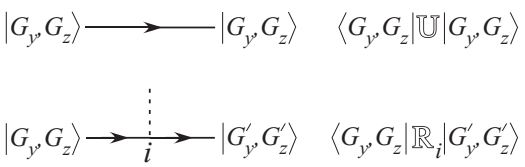

FIG. 8. Feynman rules for the diagrammatic expansion of the Casimir energy, following Ref. [45]. In our notation, plane-wave states are indexed by their reciprocal lattice vector $\mathbf{G}_\perp = (G_y, G_z)$; frequency, polarization, and the conserved reduced Bloch vector $\mathbf{k}_\perp$ are suppressed as our focus is on nonspecular (i.e., $\mathbf{G}_\perp$ not conserved) reflections. Here $\mathbb{U}$ is the free-space translation matrix, and $\mathbb{R}_i$ is the scattering matrix for object i (= 1,2 for our case). Primes on the polarizations (e.g., y') denote distinct wave vectors.

with

$$A = L_{14}L_{41}, \quad B = L_{23}L_{32}, \quad C = L_{14}L_{42}L_{23}L_{31}.$$

Finally, the elements L_{ij} are defined in terms of the permittivity tensor as

$$L_{14} = \frac{k_{z'}^2}{\omega^2}\varepsilon_{||} - 1, \quad L_{23} = 1,$$
$$L_{31} = -L_{42} = (\varepsilon_\perp - \varepsilon_{||})sc,$$
$$L_{32} = -\frac{k_{z'}^2}{\omega^2} + \varepsilon_\perp c^2 + \varepsilon_{||}s^2,$$
$$L_{41} = -\varepsilon_{||}c^2 - \varepsilon_\perp s^2.$$

A careful analysis shows that Eqs. (A10) become singular at $\phi = n\frac{\pi}{2}$ for integer n. In this case, we take the limit $\phi \to n\frac{\pi}{2}$ numerically.

APPENDIX B: SUPPRESSION OF NON-SPECULAR SCATTERING

In this section we give a proof that nonspecular scatterings (i.e., those not conserving the perpendicular wave vector $\mathbf{k}_\perp + \mathbf{G}_\perp$) are greatly suppressed for crossed slabs relative to aligned slabs. This explains the wide range of validity for the specular-reflection approximation for crossed slabs. The proof is a

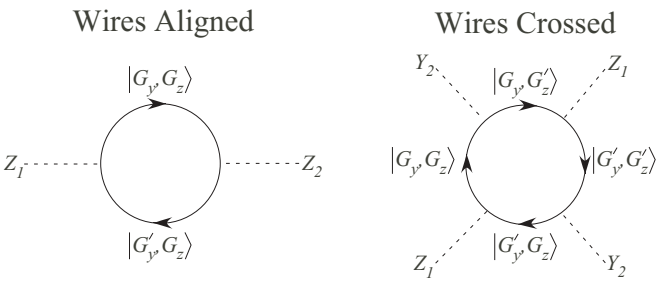

FIG. 9. Lowest-order diagrams representing the contribution of nonspecular scattering events to the Casimir energy, constructed using the rules of Fig. 8. Because we are measuring the energy of interaction between two objects, successive interaction vertices must involve different objects. On the left, when both objects 1 and 2 are directed along the z axis, a nonspecular event can occur in a two-vertex diagram. However, when the wires are crossed, the lowest-order allowed nonspecular process involves a four-vertex diagram.

straightforward application of a recently developed diagrammatic expansion for the Casimir force [45]. In this framework, the log det expression of Eq. (2) is reexpressed as Tr log and expanded in a power series. Each term in the power series can be computed via a set of Feynman rules, shown in Fig. 8. For sufficiently large separations, this series is rapidly convergent.

Each scattering event is represented as the process $|G_x, G_z\rangle \to |G'_x, G'_z\rangle$, where G_x, G_z represent the perpendicular wave vector of the plane wave. We suppress both the frequency and reduced Bloch vector $\mathbf{k}_\perp$ (which are both conserved in the scattering process), and the polarization p (which is not relevant to our analysis of nonspecular reflection). Each object is represented as a pair indicating the object alignment (Y, Z) and object index $(1,2)$. The key point is that, due to translation invariance, the scattering matrix for a Z object is proportional to $\delta(G_z - G'_z)$, and for a Y object is proportional to $\delta(G_y - G'_y)$. Further, the free-space propagator is diagonal in the plane-wave basis and thus conserves both G_y and G_z. Successive interaction vertices in a diagram must involve distinct objects as external insertions; therefore, for the crossed configuration, a plane wave must scatter twice as many times to return to its original state in the lowest-order diagram relative to the aligned configuration. Example lowest-order diagrams are shown in Fig. 9. We find that for aligned (e.g., ZZ) slabs, the lowest-order diagram involving nonspecular reflection involves two vertices, while for crossed slabs it involves four vertices. Since each propagator represents an exponential attenuation, and each scattering event multiplication by a number of magnitude less than unity, this implies that nonspecular interactions are greatly suppressed for crossed slabs.

[1] M. P. Hertzberg, R. L. Jaffe, M. Kardar, and A. Scardicchio, Phys. Rev. Lett. **95**, 250402 (2005).

[2] R. B. Rodrigues, P. A. Maia Neto, A. Lambrecht, and S. Reynaud, Europhys. Lett. **75**, 822 (2006).

[3] A. Rodriguez, M. Ibanescu, D. Iannuzzi, F. Capasso, J. D. Joannopoulos, and S. G. Johnson, Phys. Rev. Lett. **99**, 080401 (2007).

[4] T. Emig, Phys. Rev. Lett. **98**, 160801 (2007).

[5] A. W. Rodriguez, J. D. Joannopoulos, and S. G. Johnson, Phys. Rev. A **77**, 062107 (2008).

[6] F. S. S. Rosa, D. A. R. Dalvit, and P. W. Milonni, Phys. Rev. Lett. **100**, 183602 (2008).

[7] S. J. Rahi and S. Zaheer, Phys. Rev. Lett. **104**, 070405 (2010).

[8] M. Levin, A. P. McCauley, A. W. Rodriguez, M. T. Homer Reid, and S. G. Johnson, Phys. Rev. Lett. **105**, 090403 (2010).

[9] S. de Man, K. Heeck, R. J. Wijngaarden, and D. Iannuzzi, Phys. Rev. Lett. **103**, 040402 (2009).

[10] A. A. Feiler, L. Bergstrom, and M. W. Rutland, Langmuir **24**, 2274 (2008).

[11] J. Munday, F. Capasso, and V. A. Parsegian, Nature (London) **457**, 170 (2009).

[12] A. W. Rodriguez, A. P. McCauley, D. Woolf, F. Capasso, J. D. Joannopoulos, and S. G. Johnson, Phys. Rev. Lett. **104**, 160402 (2010).

[13] B. V. Derjaguin, I. I. Abrikosova, and E. M. Lifshitz, Q. Rev., Chem. Soc. **10**, 295 (1956).

[14] T. Kushta and K. Yasumoto, Prog. Electromagn. Res. **29**, 69 (2000).

[15] K. Yasumoto and H. Jia, in *Wave Propagation, Scattering and Emission in Complex Media*, edited by Y. Jin (World Scientific, Singapore, 2004), pp. 225–249.

[16] S. J. Rahi, T. Emig, N. Graham, R. L. Jaffe, and M. Kardar, Phys. Rev. D **80**, 085021 (2009).

[17] F. S. S. Rosa, D. A. R. Dalvit, and P. W. Milonni, Phys. Rev. A **78**, 032117 (2008).

[18] I. E. Dzyaloshinskiĭ, E. M. Lifshitz, and L. P. Pitaevskiĭ, Adv. Phys. **10**, 165 (1961).

[19] R. Zhao, J. Zhou, T. Koschny, E. N. Economou, and C. M. Soukoulis, Phys. Rev. Lett. **103**, 103602 (2009).

[20] S. J. Rahi, M. Kardar, and T. Emig, Phys. Rev. Lett. **105**, 070404 (2010).

[21] A. P. McCauley, R. Zhao, M. T. Homer Reid, A. W. Rodriguez, J. Zhuo, F. S. S. Rosa, J. D. Joannopoulos, D. A. R. Dalvit, C. M. Soukoulis, and S. G. Johnson, Phys. Rev. B **82**, 165108 (2010).

[22] S. J. van Enk, Phys. Rev. A **52**, 2569 (1995).

[23] C.-G. Shao, A.-H. Tong, and J. Luo, Phys. Rev. A **72**, 022102 (2005).

[24] J. N. Munday, D. Iannuzzi, Y. Barash, and F. Capasso, Phys. Rev. A **71**, 042102 (2005).

[25] O. Kenneth and S. Nussinov, Phys. Rev. D **63**, 121701 (2001).

[26] A. W. Rodriguez, D. Woolf, P.-C. Hui, E. Iwase, A. P. McCauley, F. Capasso, M. Loncar, and S. G. Johnson, e-print arXiv:1101.4237.

[27] D. Morecroft, J. K. W. Yang, S. Schuster, K. K. Berggren, Q. Xia, W. Wu, and R. S. Williams, J. Vac. Sci. Technol. B **27**, 2837 (2009).

[28] A. Lambrecht and V. N. Marachevsky, Phys. Rev. Lett. **101**, 160403 (2008).

[29] P. S. Davids, F. Intravaia, F. S. S. Rosa, and D. A. R. Dalvit, Phys. Rev. A **82**, 062111 (2010).

[30] M. T. Homer Reid, A. W. Rodriguez, J. White, and S. G. Johnson, Phys. Rev. Lett. **103**, 040401 (2009).

[31] M. T. Homer Reid, *In Preparation* (2011).

[32] A. W. Rodriguez, A. P. McCauley, J. D. Joannopoulos, and S. G. Johnson, Phys. Rev. A **80**, 012115 (2009).

[33] A. P. McCauley, A. W. Rodriguez, J. D. Joannopoulos, and S. G. Johnson, Phys. Rev. A **81**, 012119 (2010).

[34] T. Emig, N. Graham, R. L. Jaffe, and M. Kardar, Phys. Rev. Lett. **99**, 170403 (2007).

[35] O. Kenneth and I. Klich, Phys. Rev. B **78**, 014103 (2008).

[36] P. A. Maia Neto, A. Lambrecht, and S. Reynaud, Phys. Rev. A **78**, 012115 (2008).

[37] V. A. Parsegian and G. H. Weiss, J. Adhes. **3**, 259 (1972).

[38] Y. Barash and V. L. Ginzburg, Usp. Fiz. Nauk **116**, 5 (1975) [Sov. Phys. Usp. **18**, 305 (1975)].

[39] Y. Barash, Izv. Vyssh. Uchebn. Zaved. Radiofiz. **21**, 1637 (1978) [Radiophysics and Quantum Electronics **21**, 1138 (1978)].

[40] T. G. Philbin and U. Leonhardt, Phys. Rev. A **78**, 042107 (2008).

[41] A. Milling, P. Mulvaney, and I. Larson, J. Colloid Interface Sci. **180**, 460 (1996).
[42] L. Bergstrom, Adv. Colloid Interface Sci. **70**, 125 (1997).
[43] O. Kenneth and I. Klich, Phys. Rev. Lett. **97**, 160401 (2006).
[44] J. B. Pendry, A. J. Holden, W. J. Stewart, and I. Youngs, Phys. Rev. Lett. **76**, 4773 (1996).
[45] M. F. Maghrebi, Phys. Rev. D **83**, 045004 (2011).
[46] S. K. Lamoreaux, Phys. Rev. Lett. **78**, 5 (1997).
[47] U. Mohideen and A. Roy, Phys. Rev. Lett. **81**, 4549 (1998).
[48] M. Brown-Hayes, D. A. R. Dalvit, F. D. Mazzitelli, W. J. Kim, and R. Onofrio, Phys. Rev. A **72**, 052102 (2005).
[49] Q. Wei, D. A. R. Dalvit, F. C. Lombardo, F. D. Mazzitelli, and R. Onofrio, Phys. Rev. A **81**, 052115 (2010).
[50] S. de Man, K. Heeck, R. J. Wijngaarden, and D. Iannuzzi, J. Vac. Sci. Technol. B **28**, C4A25 (2010).
[51] S. de Man, K. Heeck, and D. Iannuzzi, Phys. Rev. A **82**, 062512 (2010).
[52] S. G. Johnson, e-print arXiv:1007.0966[quant-ph]; *Casimir Physics*, Lecture Notes in Physics, edited by D. A. R. Dalvit, P. W. Milonni, D. C. Roberts, and F. S. S. Rosa (Springer, New York) (in press).
[53] A. Rodriguez, M. Ibanescu, D. Iannuzzi, J. D. Joannopoulos, and S. G. Johnson, Phys. Rev. A **76**, 032106 (2007).
[54] S. Pasquali and A. C. Maggs, Phys. Rev. A **79**, 020102(R) (2009).
[55] M. G. Moharam, E. B. Grann, D. A. Pommet, and T. K. Gaylord, J. Opt. Soc. Am. A **12**, 1077 (1995).
[56] P. Bienstman and R. Baets, Opt. Quantum Electron. **33**, 327 (2001).
[57] J. A. Stratton, *Electromagnetic Theory* (McGraw-Hill, New York, 1941).
[58] R. Büscher and T. Emig, Phys. Rev. A **69**, 062101 (2004).
[59] L. D. Landau, E. M. Lifshitz, and L. P. Pitaevskiĭ, *Electrodynamics of Continuous Media*, Vol. 8 (Pergamon Press, Oxford, 1960).